Intense large-scale motions in zero and adverse pressure gradient turbulent boundary layers

M. Shehzad[1,*], B. Sun[1], D. Jovic[1], Y. Ostovan[2], C. Cuvier[2], J.M. Foucaut[2], C. Willert[3], C. Atkinson[1], J. Soria[1]

1: Laboratory for Turbulence Research in Aerospace & Combustion (LTRAC) Department of Mechanical and Aerospace Engineering, Monash University, Victoria 3800, Australia
2: CNRS, Laboratoire de Mécanique des fluides de Lille Kampé de Fériet, Villeneuve d'Ascq, France
3: German Aerospace Center (DLR), Institute of Propulsion Technology, Köln, Germany
*Corresponding author: Muhammad.shehzad@monash.edu

ABSTRACT

Proper orthogonal decomposition (POD) is used to study coherent structures in wall-bounded turbulent flows. The present study uses POD in turbulent boundary layers to determine the contributions of the intense large-scale motions (LSMs) to the Reynolds stresses. This study uses the 2C-2D PIV measurements of zero pressure gradient turbulent boundary layers (ZPG-TBL) at $Re_{\delta_2} = 7,750$, and adverse pressure gradient turbulent boundary layer (APG-TBL) at $\beta = 2.27$ and $Re_{\delta_2} = 16,240$, where Re_{δ_2} is the momentum thickness based Reynolds number and β is the Clauser's pressure gradient parameter. The measurements were obtained in the Laboratoire de Mécanique des Fluides de Lille (LMFL) High-Reynolds-Number (HRN) Boundary Layer Wind Tunnel, Lille, France. The snapshots of the flow field are segregated into those dominated by the intense and mild LSMs based on the intensity of the temporal coefficients of the first POD mode. The intense LSMs are further decomposed into high-momentum (HM) and low-momentum (LM) motions. The relative contributions of the HM motions to the Reynolds stresses are larger near the wall as compared to the LM motions. At the wall-normal distance of the displacement thickness (δ_1), HM and LM motions have similar contributions. Beyond δ_1, the LM motions have larger contributions with their peaks located closer to the displacement thickness height. This shows that in the presence of an APG, the turbulence activity is shifted closer to the displacement thickness height.

1. Introduction

In wall-bounded flows, LSMs are defined as coherent patterns that dominate the log layer and are characterized as alternating regions of high- and low-momentum (Kline et al., 1967). These structures also greatly influence the near-wall region as they superimpose onto the near-wall small scale motions and hence, leave their footprints at the wall (Hutchins & Marusic, 2007). Harun et al. (2013) observed that the large scale structures are energized from the wall to the boundary

layer edge in an adverse pressure gradient turbulent layer (APG-TBL) and that the amplitude modulation of near-wall small scales by the LSMs increases with an increasing APG. Bross et al. (2019) observed that the high-momentum LSMs in the buffer- and log-layer region of an APG-TBL are associated with positive fluctuating wall-shear stress, while the low-momentum LSMs are associated with negative fluctuating wall-shear stress.

The snapshots of the flow field that are dominated by the intense LSMs are segregated from the snapshots dominated by the mild LSMs using proper orthogonal decomposition (POD). POD, first used in fluid dynamics by Lumley (1967), is a generalization of the conventionally used Fourier power spectral analysis and is used to investigate the TKE distribution as a function of scales in a TBL flow that is inhomogeneous in the streamwise direction (Liu et al., 2001).

As described by Wu (2014), the velocity fields dominated by the intense LSMs are identified as snapshots for which the magnitudes of the temporal coefficients of the most energetic POD mode are larger than the standard deviation of all temporal coefficients. The snapshots dominated by the intense LSMs are further classified into the high-momentum ($u' > 0$) and low-momentum ($u' < 0$) where u' represents the streamwise velocity fluctuations. For a detailed description of the POD method and classification of the intense LSMs, see Shehzad et al. (2021).

This paper presents the use of POD in the segregation of a fluctuating flow field into subsets that are dominated by the intense LSMs or the mild LSMs. The intense LSMs are further divided into the high-momentum (HM) and the low-momentum (LM) motions. The outer-scaled Reynolds stresses conditioned on the HM and LM motions are compared among the ZPG-TBL and the APG-TBL.

2. Proper orthogonal decomposition (POD)

In this study, the snapshot-POD, which was introduced by Sirovich (1987), is used to extract modes based on optimizing the mean square of the fluctuating velocity. A brief description of the POD method is as follows:

Consider a set of fluctuating velocity fields $\overline{\overline{\boldsymbol{u'}}}(x, y, t)$ given by

$$\overline{\overline{\boldsymbol{u'}}}(x, y, t) = [\boldsymbol{u'}(x, y, t_1) \quad \boldsymbol{u'}(x, y, t_2) \quad ... \quad \boldsymbol{u'}(x, y, t_N)] \in \mathbb{R}^{M \times N}, \quad M \gg N, \tag{1}$$

where N is the number of snapshots, *i.e.* the velocity fields, and M is the number of data points in each snapshot, which is equal to the number of velocity components multiplied by the number of grid points, and

$$\boldsymbol{u'}(x, y, t) = \begin{bmatrix} u'(x, y, t) \\ v'(x, y, t) \end{bmatrix}$$

$\overline{\overline{u'}}(x, y, t)$ can be written as

$$\overline{\overline{u'}}(x, y, t) = \sum_{i=1}^{N} \psi_i(t)\phi_i(x, y) \tag{2}$$

where $\phi_i(x, y)$ is the ith spatial mode and $\psi_i(t)$ is the set of the corresponding temporal coefficients. Defining the covariance matrix $\boldsymbol{R}$ of the vector $\boldsymbol{u'}(x, y, t)$ as

$$\boldsymbol{R} = \boldsymbol{X}\boldsymbol{X}^T, \quad \boldsymbol{R} \in \mathbb{R}^{M \times M} \tag{3}$$

with $\boldsymbol{X} = \overline{\overline{\boldsymbol{u'}}}$, the classical POD of Lumley (1967) yields

$$\boldsymbol{R}\phi_i = \lambda_i\phi_i, \quad \phi_i \in \mathbb{R}^M, \; i = 1, 2, \; ... \; , M \tag{4}$$

where λ_i represents the eigenvalue of the ith POD mode. In the snapshot-POD method, the matrix $\boldsymbol{X}^T\boldsymbol{X}$ is used instead of $\boldsymbol{X}\boldsymbol{X}^T$, which is much smaller in size but yields the same nonzero eigenvalues (Sirovich, 1987). Hence, we can write

$$\boldsymbol{X}^T\boldsymbol{X}\psi_i = \lambda_i\psi_i, \quad \psi_i \in \mathbb{R}^N, \tag{5}$$

The corresponding spatial mode ϕ_i can be computed as

$$\phi_i = \boldsymbol{X}\psi_i\frac{1}{\sqrt{\lambda_i}}, \tag{6}$$

which can also be written as

$$\boldsymbol{\Phi} = \boldsymbol{X}\boldsymbol{\Psi}\boldsymbol{\Lambda}^{-1/2}, \tag{7}$$

where the columns of $\boldsymbol{\Phi}$ are the vectors of the spatial modes ($\boldsymbol{\Phi} = \begin{bmatrix} \phi_1 & \phi_2 & ... & \phi_N \end{bmatrix} \in \mathbb{R}^{M \times N}$), the columns of $\boldsymbol{\Psi}$ are the vectors of temporal coefficients corresponding to each POD mode ($\boldsymbol{\Psi} = \begin{bmatrix} \psi_1 & \psi_2 & ... & \psi_N \end{bmatrix} \in \mathbb{R}^{N \times N}$) and $\boldsymbol{\Lambda}$ is the vector of eigenvalues corresponding to each POD mode ($\boldsymbol{\Lambda} = \begin{bmatrix} \lambda_1 & \lambda_2 & ... & \lambda_N \end{bmatrix} \in \mathbb{R}^N$).

The TKE of the boundary layer flow equals to half of the sum of the eigenvalues, i.e.

$$k = \frac{1}{2}\overline{\boldsymbol{u'}^2} = \frac{1}{2}\sum_{i=1}^{N} \lambda_i \tag{8}$$

◀

3. Experimental method

This study uses the 2C-2D PIV measurements of an APG-TBL that were taken in the $x - y$ plane in the LMFL HRN wind tunnel. This facility has a 2-m wide, 1-m high and 20.6-m long test section. A schematic diagram of the LMFL wind tunnel is shown in figure 1 with three sections that have different pressure conditions: ZPG, favourable pressure gradient (FPG) and APG. The APG-TBL measurements cover about 21δ in the streamwise direction and from 0.02δ to 1.45δ in the wall-normal direction. These measurements were obtained using 16 sCMOS cameras in a 3.466 m long continuous field of view (FOV) and were used in the characterization of a high-Reynolds-number APG-TBL developing over considerably long regions (Cuvier et al., 2017). The FOV of these measurements is highlighted in figure 1. For the complete experimental details of this APG-TBL, see Cuvier et al. (2017), where these measurements were originally presented.
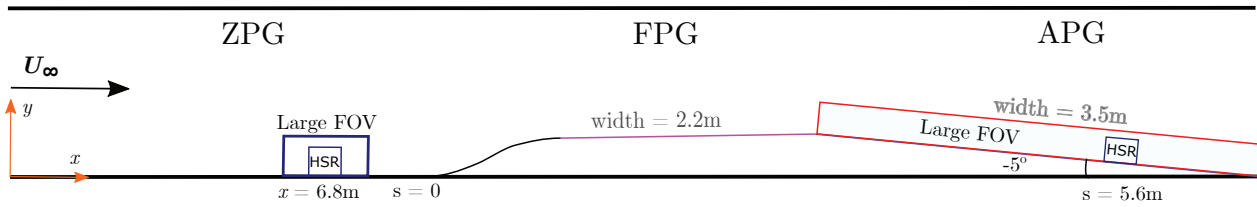

Figure 1. Schematic of the test section in the LML Wind Tunnel. Figure adapted from Cuvier et al. (2017).

To compare the first- and second-order statistics of the current APG-TBL with a ZPG-TBL, the 2C-2D PIV measurements of the latter taken in the $x - y$ plane of the same experimental facility are also included. The ZPG-TBL measurements cover about 2.61δ in the streamwise direction, and from 0.02δ to 3.12δ in the wall-normal direction. The experimental and PIV analysis parameters of the current APG-TBL are presented in table 1.

The current measurements of both TBLs do not cover the region from the wall to the end of the buffer layer. Therefore, the inner-layer measurements of two TBLs obtained in the same location of the same facility as the current TBLs, have also been included in the comparison of the first and second-order statistics. These inner-layer measurements have a higher spatial resolution (HSR) in the wall-normal direction and were taken at a time different to the outer-layer measurements. The HSR measurements of the ZPG-TBL and the APG-TBL, when compared to outer-layer measurements, are approximately 5 times more spatially resolved in the streamwise direction and more than 14 times in the wall-normal direction, respectively. For the complete experimental details of the inner-layer (*i.e.* HSR) measurements, the reader is referred to Shehzad et al. (2021).

The boundary layer parameters for both TBLs are adopted from Cuvier et al. (2017) and presented in table 2.

Table 1. PIV analysis parameters. Source for the outer-layer measurements of the APG-TBL: Cuvier et al. (2017).

Measurement	ZPG-TBL	APG-TBL
Inflow Velocity (m/s)	9	9
Viscous length scale l^+ (μm)	42	44
FOV ($l^+ \times l^+$)	$6,342 \times 7,218$	$78,847 \times 5,801$
(pixels $\times$ pixels)	$2,338 \times 2,786$	$32,494 \times 2,391$
(mm $\times$ mm)	266×317	$3,466 \times 254$
Grid spacing ($l^+ \times l^+$)	25×25	24×24
(pixels $\times$ pixels)	7×7	10×10
IW size ($l^+ \times l^+$)	57×57	58×58
(pixels $\times$ pixels)	16×16	24×24
Frequency (Hz)	5	4
Number of samples	10,000	30,000
Vector field size	334×398	$3,250 \times 238$

Table 2. The boundary layer parameters at the middle of the FOV for the ZPG-TBL and at $s = 5.6$ m for the APG-TBL.

	ZPG-TBL	APG-TBL
Edge velocity, U_e (m/s)	9.64	11.59
Boundary layer thickness, δ (mm)	102	175
Displacement thickness, δ_1 (mm)	16.4	33.5
Momentum thickness, δ_2 (mm)	12.0	21.0
Shape factor, H	1.37	1.45
Momentum thickness based Reynolds number, Re_{δ_2}	7,750	16,240
Clauser's pressure gradient parameter, β	-	2.27

4. First- and second-order statistics

The mean velocity profiles of both TBLs, scaled with the outer variables δ_1 and U_e, are shown in figure 2(a). Likewise, the Reynolds stress profiles are also scaled with outer variables and shown in figure 2(b). As it is clear from these figures, the outer-layer measurements are consistent with the inner-layer HSR measurements. The ZPG-TBL has one inner peak in Reynolds streamwise stresses

and no outer peak. The APG-TBL has an outer peak located around $y = 1.3\delta_1$ that is as strong as the inner peak. The Reynolds wall-normal and shear stresses in the outer region have outer peaks in the APG-TBL and plateaus in the ZPG-TBL.
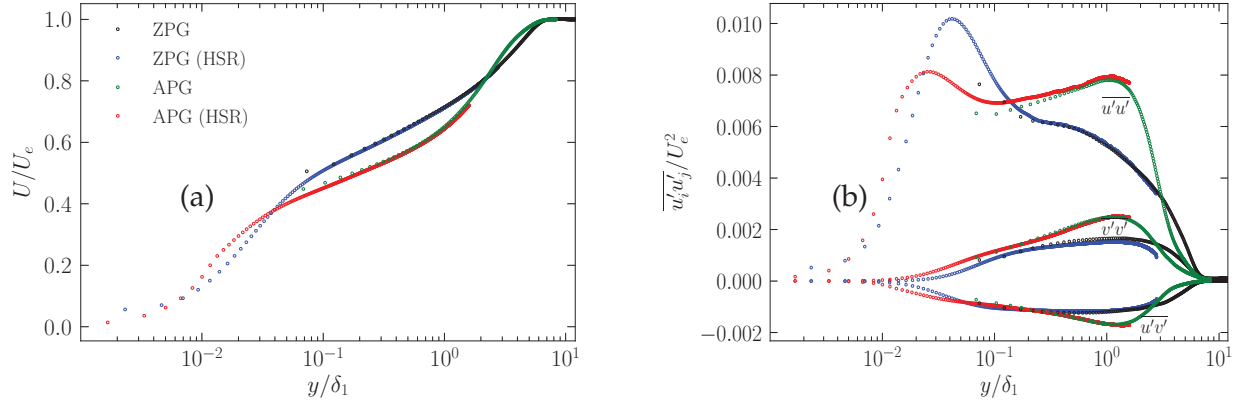

Figure 2. The outer-scaled profiles of the (a) mean streamwise velocity and (b) the Reynolds stresses.

5. Classification of large-scale motions

POD is used to analyse the intense LSMs in the ZPG- and APG-TBLs. Since all snapshots contribute differently to the first and every other POD mode, those fields which have the largest contributions to the large scales of the first mode ϕ_1 can be characterized as snapshots dominated by intense LSMs. The extent of the contribution of each velocity field to the first spatial mode is reflected by the magnitude of its temporal coefficient corresponding to the first mode.

The fluctuating flow-field is divided into two subsets: one dominated by the intense LSMs or the other by the mild LSMs, based on the magnitude of the temporal coefficients of the most energetic POD mode, ψ_1. A threshold $K\sigma_{\psi_1}$ is used as a discriminator between the intense LSMs and mild LSMs where K is an arbitrary constant. Given that the temporal coefficients of the first POD mode have a Euclidean norm of 1, $K = 1$ is chosen for the classification of the intense LSMs into the high and low-momentum events. The criterion of segregation of the intense LSMs into the HM and LM motions is as follows.

If the streamwise component of the first mode is positive (*i.e.* $\phi_{1_u} > 0$), the snapshots of the flow field $\mathbf{F}$ which have their temporal coefficients in the first POD mode (ψ_1) larger than σ_{ψ_1}, are identified as those with dominant high-momentum motions (**H**) and those with ψ_1 smaller than $-\sigma_{\psi_1}$ are identified as those with dominant low-momentum motions (**L**).

If $\mathbf{F}$ is the set of all fluctuating velocity fields, $\mathbf{F}(\psi_1 \geq \sigma_{\psi_1}) \rightarrow \mathbf{H}$ and $\mathbf{F}(\psi_1 < -\sigma_{\psi_1}) \rightarrow \mathbf{L}$. Conversely, if $\phi_{1_u} < 0$, the snapshots of the flow field $\mathbf{F}$ with $\psi_1 > K\sigma_{\psi_1}$ are identified as fields with dominant LM events (**L**), and those with $\psi_1 < -K\sigma_{\psi_1}$ as fields with dominant HM events (**H**), *i.e.* $\mathbf{F}(\psi_1 > \sigma_{\psi_1}) \longrightarrow \mathbf{L}$ and $\mathbf{F}(\psi_1 \leq -\sigma_{\psi_1}) \longrightarrow \mathbf{H}$.

The distributions of the temporal coefficients of velocity fields with LSMs for the ZPG-TBL is shown in figure 3. The APG-TBL also has $\phi_{1_u} > 0$ and has the distribution similar to the ZPG-TBL. These distributions are of a Gaussian nature. As $\phi_{1_u} > 0$ for both ZPG- and APG-TBL, the velocity fields dominated by the high- and low-momentum intense LSMs are represented by the H (red) and L (blue) regions, respectively. In contrast, if $\phi_{1_u} < 0$, the red and blue regions would represent the low- and high momentum events, respectively. These regions are bounded by dotted lines of $\psi_{1_j} = \pm\sigma_{\psi_1}$ and solid lines of PDF ($|\psi_{1_j}| > \sigma_{\psi_1}$).
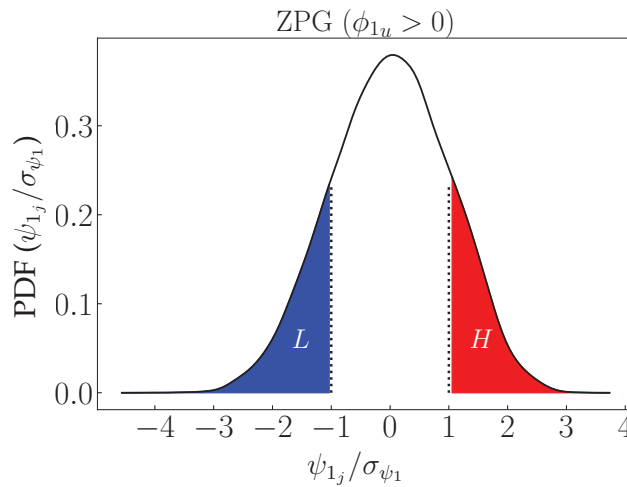

Figure 3. PDFs of the temporal coefficients corresponding to the first POD modes for the ZPG-TBL. The APG-TBL also has $\phi_{1_u} > 0$ and has the distribution similar to the ZPG-TBL.

6. Reynolds stresses conditioned on intense LSMs

Figure 4 shows the contributions of the HM and LM motions, as well as the mild LSMs to the Reynolds stresses. The contributions of the intense LSMs are the most prominent in the outer region. These are of maximum values in the Reynolds streamwise stresses, with slightly lower values in the Reynolds shear stresses, and the minimum values in the Reynolds wall-normal stress. The Reynolds stress profiles conditioned on the HM- and LM- LSMs have their cross-over point located around $y = \delta_1$. At this point, the conditional Reynolds stresses have values higher than the corresponding unconditional Reynolds stresses. Below this point, HM events contribute more to the Reynolds stresses than the LM events and further out, the opposite is the case. The differences between the unconditional Reynolds streamwise, shear, and wall-normal stresses and the corresponding conditional stresses at the cross-over points are 42.4%, 3.3%, and 25.7%, respectively. In APG-TBL, these differences are 41.1%, 2.0%, and 29.3%, respectively. When normalized by the corresponding unconditional Reynolds stresses and plotted against the wall-normal distance scaled with δ_1 as in figure 4, the HM and LM profiles show similar distributions for the two TBLs below the cross over points. Beyond the cross-over point, however, the peaks in the HM and LM profiles in APG-TBL are shifted closer to $y = \delta_1$ when compared to the ZPG-TBL. This shows that the tur-

bulence shifted closer to $y = \delta_1$ when an APG is imposed. Furthermore, the combined effect of the HM and LM motions is similar between the two TBLs except in Reynolds shear stress where the mild LSMs have a 23% reduced contribution in ZPG-TBL as compared to the 18% in APG-TBL.
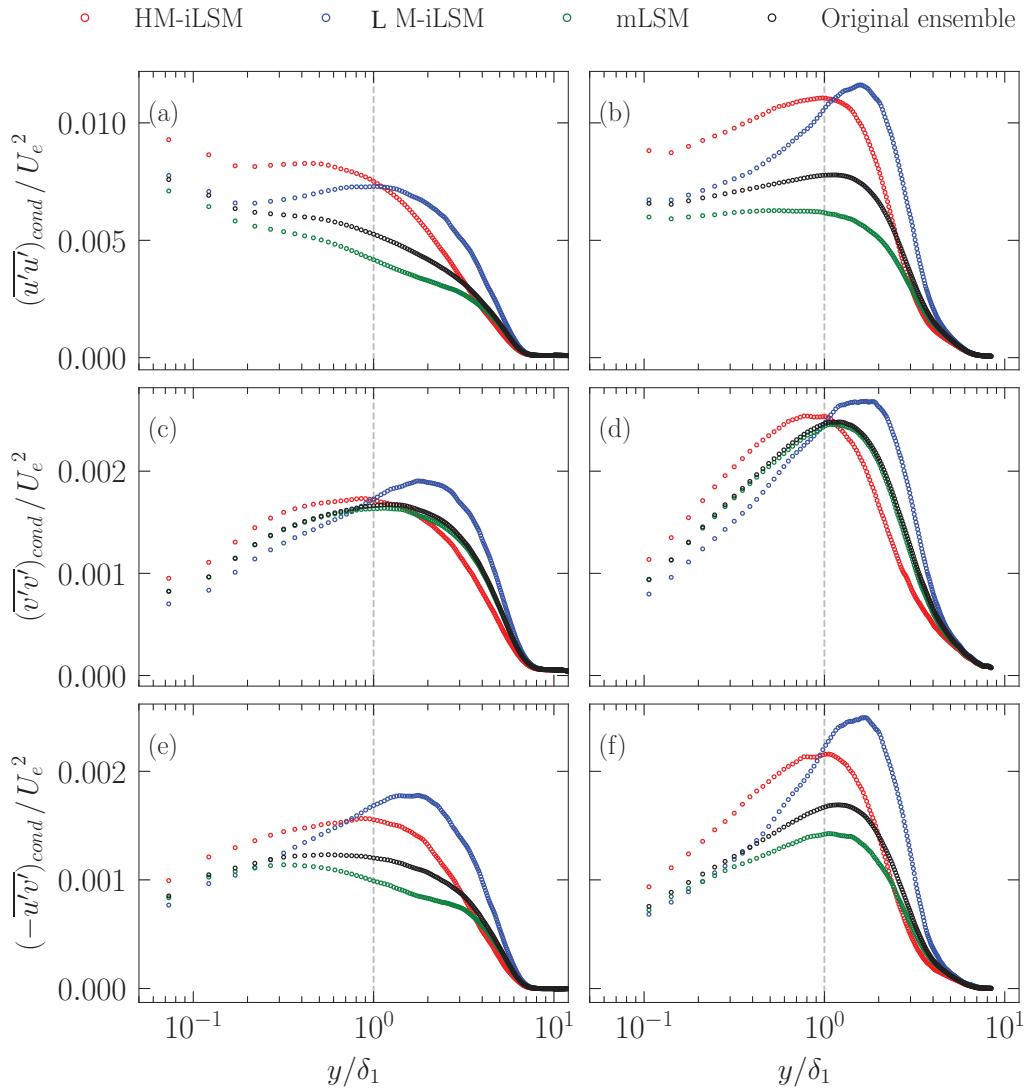

Figure 4. Conditionally averaged statistics of high- and low-momentum intense LSMs and mild LSMs. The black symbols show the unconditional Reynolds stresses. ZPG-TBL (a, c, e), and APG-TBL (b, d, f). The dashed grey line indicates $y = \delta_1$. The notation 'HM-iLSM' represents the HM intense LSMs, and the 'mLSM' represents the mild LSMs.

7. Conclusion

The contributions of the high-momentum and low-momentum intense large-scale motions to the Reynolds stresses are investigated. The Reynolds stress profiles conditioned on the HM and LM

intense LSMs have their crossover point always at $y \approx \delta_1$, irrespective of the pressure gradient imposed on the TBL. At this point, the conditional Reynolds stresses have higher values than the corresponding unconditional Reynolds stresses. Below this cross-over point, the HM events contribute more to the Reynolds stresses than the LM events and further out, the opposite is the case. Furthermore, the peaks in the relative HM and LM profiles are shifted closer to $y = \delta_1$ with increasing APG. This shows that under APG, the activity is shifted to the vicinity that is closer to $y = \delta_1$.

References

Bross, M., Fuchs, T., & Kähler, C. J. (2019). Interaction of coherent flow structures in adverse pressure gradient turbulent boundary layers. *Journal of Fluid Mechanics*, *873*, 287–321.

Cuvier, C., Srinath, S., Stanislas, M., Foucaut, J., Laval, J., Kähler, C., . . . others (2017). Extensive characterisation of a high Reynolds number decelerating boundary layer using advanced optical metrology. *Journal of Turbulence*, *18*(10), 929–972.

Harun, Z., Monty, J. P., Mathis, R., & Marusic, I. (2013). Pressure gradient effects on the large-scale structure of turbulent boundary layers. *Journal of Fluid Mechanics*, *715*, 477–498.

Hutchins, N., & Marusic, I. (2007). Evidence of very long meandering features in the logarithmic region of turbulent boundary layers. *Journal of Fluid Mechanics*, *579*, 1–28.

Liu, Z., Adrian, R., & Hanratty, T. (2001). Large-scale modes of turbulent channel flow: transport and structure. *Journal of Fluid Mechanics*, *448*, 53.

Lumley, J. L. (1967). The structure of inhomogeneous turbulent flows. *Atmospheric turbulence and radio wave propagation*.

Shehzad, M., Sun, B., Jovic, D., Ostovan, Y., Cuvier, C., Foucaut, J.-M., . . . Soria, J. (2021). Investigation of large scale motions in zero and adverse pressure gradient turbulent boundary layers using high-spatial-resolution particle image velocimetry. *Experimental Thermal and Fluid Science*, *129*, 110469. Retrieved from https://www.sciencedirect.com/science/article/pii/S0894177721001163 doi: https://doi.org/10.1016/j.expthermflusci.2021.110469

Sirovich, L. (1987). Turbulence and the dynamics of coherent structures. parts I-III. *Quarterly of applied mathematics*, *XLV*, 561–590.

Wu, Y. (2014). A study of energetic large-scale structures in turbulent boundary layer. *Physics of Fluids*, *26*(4), 045113.